AIAA JOURNAL
Vol. 32, No. 10, October 1994

Projection Method for Viscous Incompressible Flow on Quadrilateral Grids

John B. Bell*
Lawrence Livermore National Laboratory, Livermore, California 94550
and
Jay M. Solomon† and William G. Szymczak†
Naval Surface Warfare Center, Silver Spring, Maryland 20903

This paper describes a second-order projection method for the incompressible Navier-Stokes equations on multiply connected domains with a logically rectangular quadrilateral grid. The method uses a second-order fractional step scheme in which one first solves diffusion-convection equations to determine intermediate velocities which are then projected onto the space of divergence-free vector fields. The spatial discretizations are accomplished by formally transforming the equations to a computational space with a uniform grid. The diffusion, pressure gradient, and divergence terms are discretized using standard finite difference approximations. The convection terms are discretized using a second-order Godunov method that provides a robust discretization of these terms at high Reynolds number. Numerical results are presented illustrating the performance of the method.

I. Introduction

THIS paper describes a second-order projection method for the time-dependent, incompressible Navier-Stokes equations

$$U_t + (U\cdot\nabla)U = \varepsilon\Delta U - \nabla p \tag{1}$$

$$\nabla\cdot U = 0 \tag{2}$$

on a logically rectangular quadrilateral grid where $\varepsilon^{-1} = Re$ is the Reynolds number, U the velocity vector, and p the pressure. The method is a generalization of a second-order projection method first introduced by Bell et al.[1,2] and subsequently developed by Bell et al.[3] for the study of shear flows. The basic approach is a second-order fractional step method, similar to a method introduced by van Kan,[4] in which Eq. (1) is solved with the pressure term lagged to determine an intermediate velocity field that does not satisfy Eq. (2). This intermediate velocity field is then decomposed into solenoidal and gradient components which determine the new velocity and an update for the pressure, respectively. The method also incorporates second-order Godunov-type differencing of the nonlinear terms in Eq. (1) that provides a robust, high-resolution discretization at high Reynolds number.

In deriving the extension to quadrilateral grids we will formally assume that the grid points are defined by a transformation Φ from a computational space $\Xi = (\xi, \eta)$ to the physical space $X = (x, y)$; i.e.,

$$X = \Phi(\Xi)$$

When we transform the Navier-Stokes equations to the computational coordinate system we obtain

$$JU_t + [\bar{U}\cdot\nabla_\Xi]U = \varepsilon\nabla_\Xi\cdot[(1/J)TT^t\nabla_\Xi U] - T^t\nabla_\Xi p \tag{3}$$

$$\nabla_\Xi\cdot\bar{U} = 0 \tag{4}$$

where $J = \det\nabla_\Xi\Phi$, $\bar{U} = TU$, and

$$T \equiv J[\nabla_\Xi\Phi]^{-1} = \begin{bmatrix} y_\eta & -x_\eta \\ -y_\xi & x_\xi \end{bmatrix}$$

Here, ∇_Ξ and $\nabla_\Xi\cdot$ denote the gradient and divergence operators in computational space. The quadrilateral-grid algorithm is defined in terms of the transformed equations (3) and (4). The metric coefficients introduced in the transformation are evaluated using appropriate differences of grid-point locations. These difference approximations are chosen so that the method satisfies a freestream preservation property that guarantees exact treatment of a uniform flow independent of the grid variation. The algorithm is designed to be second-order accurate for smooth flow provided the mapping Φ is smooth. The higher order Godunov treatment of the convective terms and freestream preservation ensure the robustness of the algorithm for rough data and for nonsmooth grid variation. The algorithm does not explicitly use the mapping Φ; all that is actually required are the locations of the grid points in physical space. Consequently, any body conforming grid generation algorithm can be used to generate the grids.

In the next section we describe the basic fractional-step approach used for the temporal discretization in the algorithm. In Sec. III we discuss the spatial discretization of the diffusion-convection equation (3) and in Sec. IV we describe a discrete algorithm for approximating the projection. In the last section we present computational results for flow in a channel with a constriction and flow over a cylinder.

II. Temporal Discretization

In this section we describe the second-order fractional step formulation used in the quadrilateral-mesh projection algorithm. This formulation, which provides the basic temporal discretization, is the same as that used by Bell et al.[2] Projection methods, originally developed by Chorin,[5] are fractional step methods based on the decomposition of vector fields into a divergence-free component and the gradient of a scalar field. More precisely, any vector field V can be uniquely written as $V = U_d + \nabla\phi$ where ϕ is a scalar and U_d is divergence free and satisfies specified boundary conditions. Furthermore, one can define an orthogonal projection P such that $U_d = PV$ and $\nabla\phi = (I-P)V$. (See Temam[6] for a more detailed discussion of the projection.) For quadrilateral grids, the algorithm will be de-

Received April 21, 1993; revision received Feb. 10, 1994; accepted for publication Feb. 22, 1994. This paper is declared a work of the U.S. Government and is not subject to copyright protection in the United States.

*Director, Center for Computational Sciences and Computing, P.O. Box 808.

†Mathematician, Information Sciences and Systems Branch, Code B44. Member AIAA.

fined in terms of the computational space where the vector-field decomposition becomes

$$V = U_d + (1/J)T^t \nabla_\Xi \phi$$

where U_d satisfies Eq. (4).

Using the projection we can rewrite the Navier-Stokes equations (3) and (4) in the equivalent form

$$U_t = P\left[\frac{1}{J}\left\{\varepsilon\nabla_\Xi \cdot \left(\frac{1}{J}TT^t\nabla_\Xi U\right) - [\bar{U}\cdot\nabla_\Xi]\,U\right\}\right] \tag{5}$$

Equation (5) describes the evolution of U in terms of a nonlinear functional of U; the pressure has been eliminated from the system. Thus, the pressure in Eqs. (3) and (4) represents the gradient component of the vector field that is projected in Eq. (5); i.e.,

$$\frac{1}{J}T^t\nabla_\Xi p = (I-P)\left[\frac{1}{J}\left\{\varepsilon\nabla_\Xi \cdot \left(\frac{1}{J}TT^t\nabla_\Xi U\right) - [\bar{U}\cdot\nabla_\Xi]\,U\right\}\right]$$

For the basic temporal discretization, we assume that we are given an approximation to U^n. Furthermore, we assume that we have already computed a second-order time-centered approximation to the nonlinear terms $[(\bar{U}\cdot\nabla_\Xi)U]^{n+1/2}$. (A Godunov-type procedure for computing this approximation is described in the next section.) A second-order discretization of Eq. (5) can be obtained using a Crank-Nicholson approximation

$$\frac{U^{n+1}-U^n}{\Delta t} = P\left[\frac{1}{J}\left\{\frac{\varepsilon}{2}\nabla_\Xi\cdot\,[J^{-1}TT^t\nabla_\Xi(U^n+U^{n+1})]\right.\right.$$
$$\left.\left. -[(\bar{U}\cdot\nabla_\Xi)U]^{n+1/2}\right\}\right] \tag{6}$$

However, the linear algebra problem associated with solving Eq. (6) would be extremely costly because of the nonlocal behavior of the projection.

As a less costly alternative, we construct a fractional step method that approximates Eq. (6) to second-order accuracy. To accomplish this we will assume that we are also given an approximation to $J^{-1}T^t\nabla_\Xi p^{n-1/2}$. We then compute an intermediate velocity field U^* using

$$J\frac{U^*-U^n}{\Delta t} + T^t\nabla_\Xi p^{n-1/2} = \frac{\varepsilon}{2}\nabla_\Xi\cdot\,[J^{-1}TT^t\nabla_\Xi(U^n+U^*)]$$
$$-[(\bar{U}\cdot\nabla_\Xi)U]^{n+1/2} \tag{7}$$

where U^* satisfies the same boundary conditions as U. The role of the pressure gradient term in Eq. (7) is to approximate the effect of the projection in Eq. (6). We now apply the projection to decompose U^* into divergence-free and gradient components to obtain U^{n+1} and an update for $J^{-1}T^t\nabla_\Xi p$

$$U^{n+1} = PU^* \tag{8a}$$

$$J^{-1}T^t\nabla_\Xi p^{n+1/2} = J^{-1}T^t\nabla_\Xi p^{n-1/2} + \Delta t^{-1}(I-P)\,U^* \tag{8b}$$

Equations (7) and (8) represent the fractional step scheme that we have used. The relationship between Eqs. (7) and (8) and the Crank-Nicholson scheme (6) can be seen by first observing that Eqs. (8) are equivalent to

$$\frac{U^{n+1}-U^n}{\Delta t} = P\left(\frac{U^*-U^n}{\Delta t} + J^{-1}T^t\nabla_\Xi p^{n-1/2}\right) \tag{9a}$$

$$J^{-1}T^t\nabla p^{n+1/2} = (I-P)\left(\frac{U^*-U^n}{\Delta t} + J^{-1}T^t\nabla_\Xi p^{n-1/2}\right) \tag{9b}$$

If we use Eq. (7) to replace

$$\frac{U^*-U^n}{\Delta t} + J^{-1}T^t\nabla_\Xi p^{n-1/2}$$

in Eqs. (9) we obtain

$$\frac{U^{n+1}-U^n}{\Delta t} = P\left[\frac{1}{J}\left\{\frac{\varepsilon}{2}\nabla_\Xi\cdot\,[J^{-1}TT^t\nabla_\Xi(U^n+U^*)]\right.\right.$$
$$\left.\left. -[(\bar{U}\cdot\nabla_\Xi)U]^{n+1/2}\right\}\right]$$

$$J^{-1}T^t\nabla_\Xi p^{n+1/2} = (I-P)\left[\frac{1}{J}\left\{\frac{\varepsilon}{2}\nabla_\Xi\cdot\,[J^{-1}TT^t\nabla_\Xi(U^n+U^*)]\right.\right.$$
$$\left.\left. -[(\bar{U}\cdot\nabla_\Xi)U]^{n+1/2}\right\}\right]$$

from which we can see that Eq. (8a) corresponds to Eq. (6) with U^{n+1} approximated by U^* on the right-hand side and that $J^{-1}T^t\nabla_\Xi p^{n+1/2}$ represents the gradient component of the vector field being projected.

We note that since $\nabla_\Xi p^{-1/2}$ is not available, some procedure is required to initialize the fractional step algorithm. We have chosen to simply iterate Eqs. (7) and (8) (with $\nabla_\Xi p = 0$ initially) on the first step to compute converged approximations to U^1 and $J^{-1}T^t\nabla_\Xi p^{1/2}$.

The inclusion of the $J^{-1}T^t\nabla_\Xi p^{n-1/2}$ in Eq. (7) makes the algorithm second-order accurate in time. The reader is referred to Bell et al.[1] for a more detailed discussion of the convergence behavior of the fractional step scheme. There are several alternative formulations that also give second-order temporal accuracy. Van Kan[4] proposes a similar scheme in which the pressures are not staggered in time. Kim and Moin[7] achieve second-order accuracy by modifying the boundary conditions satisfied by U^*.

Before describing the spatial discretizations used in the algorithm we will summarize the basic approach. First we solve the diffusion-convection equations (7). This is a two-step process in which we first approximate $[(\bar{U}\cdot\nabla_\Xi)U]^{n+1/2}$ using a second-order Godunov procedure. Then, we solve the two parabolic equations represented by Eq. (7) with the nonlinear term treated as a source term. In the second step of the algorithm, we apply the projection to update U and $J^{-1}T^t\nabla_\Xi p$. In Sec. IV we discuss the spatial discretization of the diffusion-convection equations that forms the first step of the algorithm. In the following section we describe the approximation of the projection.

III. Spatial Discretization

The spatial discretization is based on the staggered grid system depicted in Fig. 1. On this grid, vector quantities (U and ∇p) are defined at the grid points, denoted by ○ in the figure, and scalar quantities ($\nabla\cdot U$ and p) are defined at the cell centers, denoted by × in the figure. The transformation Φ is viewed as being defined so that the grid in computational space is composed of unit squares; i.e., $X_{ij} = \Phi(i, j)$. (Thus, the grid in computational space has $\Delta\xi = \Delta\eta = 1$ so that difference approximations are undivided.) The cell centers $X_{i+1/2,j+1/2} = (1/4)(X_{ij} + X_{i+1,j} + X_{i,j+1} + X_{i+1,j+1})$ form a dual grid that associates a cell with each of the original grid points. Differences of the dual grid-point locations are used to define metric coefficients on the primary grid, namely,

$$(X_\xi)_{ij} = (1/2)(X_{i+1/2,j+1/2} + X_{i+1/2,j-1/2} - X_{i-1/2,j+1/2} - X_{i-1/2,j-1/2})$$

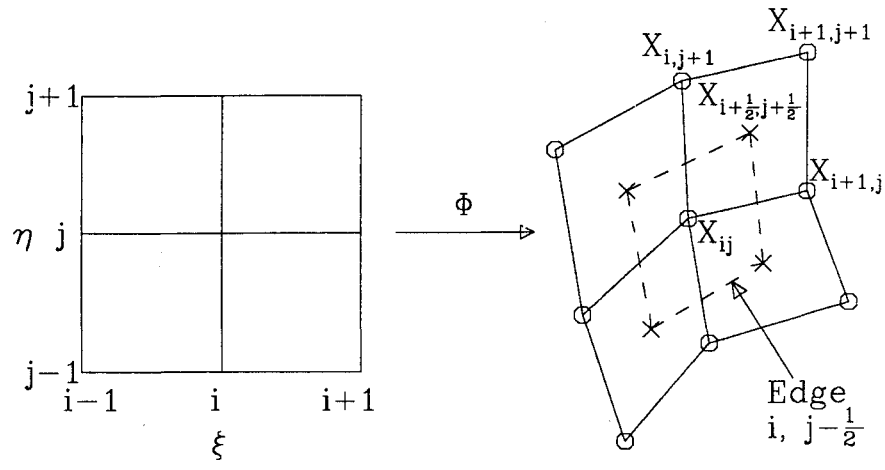

Fig. 1 Staggered grid structure.

with an analogous formula for $(X_\eta)_{ij}$. We note that with this particular choice of difference approximations for the metric coefficients, a uniform velocity field will remain divergence free on any grid (see, e.g., Ref. 8).

As noted, there are two distinct components of the spatial approximation of Eq. (7): discretization of the Laplacian used to model the diffusion terms and the second-order Godunov procedure that is used to compute $[(\bar{U}\cdot\nabla_\Xi)U]^{n+1/2}$. The discretization of the Laplacian is done using standard, finite difference approximations. The Laplacian in computational coordinates, namely, $\nabla_\Xi\cdot(J^{-1}TT^T\nabla_\Xi U)$, has the form

$$(\alpha U_\xi)_\xi + (\beta U_\xi)_\eta + (\beta U_\eta)_\xi + (\gamma U_\eta)_\eta \tag{10}$$

where

$$\alpha = J^{-1}(x_\eta^2 + y_\eta^2), \qquad \beta = -J^{-1}(x_\eta y_\xi + x_\xi y_\eta)$$

$$\gamma = J^{-1}(x_\xi^2 + y_\xi^2)$$

Each term in Eq. (10) is discretized using standard second-order differences with coefficients computed by averaging metric coefficients at grid points. The linear system associated with the parabolic equations (7) using Eq. (10) for the diffusion discretization is solved using diagonal scaling as a preconditioner for conjugate gradient iteration.

The algorithm for computing $[(\bar{U}\cdot\nabla_\Xi)U]^{n+1/2}$ is based on the unsplit, second-order upwind methods first proposed by Colella[9] and by van Leer.[10] Unlike standard upwind differencing methods, these types of schemes couple the spatial and temporal discretization by propagating information along characteristics. This approach leads to a robust higher order discretization with excellent phase-error properties. The scheme described here is a cell-centered predictor-corrector scheme. We use the cells defined by the dual grid for the discretization. In the predictor step of the algorithm, we extrapolate U along characteristics to obtain values at the cell edges at $t^{n+1/2}$. In the corrector step, we compute upwind fluxes for the velocities which are then differenced to obtain a time-centered approximation to $(\bar{U}\cdot\nabla_\Xi)U$.

Predictor

In the predictor we extrapolate along characteristics using solution values at t^n to predict values of U on cell edges at time $t^{n+1/2}$. The basis for the extrapolation is Taylor series. To second-order accuracy

$$U_{i+1/2,j}^{n+1/2,L} = U_{ij}^n + \frac{1}{2}U_{\xi,ij}^n + \frac{\Delta t}{2}U_{t,ij}^n \tag{11a}$$

$$U_{i-1/2,j}^{n+1/2,R} = U_{ij}^n - \frac{1}{2}U_{\xi,ij}^n + \frac{\Delta t}{2}U_{t,ij}^n \tag{11b}$$

$$U_{i,j+1/2}^{n+1/2,B} = U_{ij}^n + \frac{1}{2}U_{\eta,ij}^n + \frac{\Delta t}{2}U_{t,ij}^n \tag{11c}$$

$$U_{i,j-1/2}^{n+1/2,T} = U_{ij}^n - \frac{1}{2}U_{\eta,ij}^n + \frac{\Delta t}{2}U_{t,ij}^n \tag{11d}$$

The first two quantities denote the extrapolation of U to the left side of edge $i+1/2, j$ and to the right side of edge $i-1/2, j$, respectively. The last two are the extrapolation of U to the bottom side of edge $i, j+1/2$ and the top side of edge $i, j-1/2$. We now use the differential equations (3) to express the time derivatives in terms of spatial derivatives with the pressure gradient lagged to time $t^{n-1/2}$. This gives, for Eq. (11a)

$$U_{i+1/2,j}^{n+1/2,L} = U_{ij}^n + s_L\left[\frac{1}{2} - \frac{\Delta t}{2J}\bar{u}_{ij}^n\right]U_{\xi,ij}^n - \frac{\Delta t}{2J}\bar{v}_{ij}^n U_{\eta,ij}^n$$

$$+ \frac{\Delta t}{2J}\left[\varepsilon\nabla_\Xi\cdot\left(\frac{1}{J}TT^t\nabla_\Xi U\right)^n - T^t\nabla_\Xi p^{n-1/2}\right] \tag{12}$$

where s_L is 1 if $\bar{u}_{ij}^n \geq 0$ and 0 otherwise. Analogous formulas are used for Eqs. (11b–11d). In Eq. (12), the derivative normal to the edge U_ξ is evaluated using central differences with monotonicity constraints which we denote by $(\Delta_\xi U)_{ij}$. The transverse derivative is evaluated using an upwind difference approximation. More precisely, if $\bar{v}_{ij} \geq 0$,

$$U_{\eta,ij} = U_{ij} - U_{ij-1} + \left[\frac{1}{2} - \frac{\Delta t\bar{v}_{ij}}{2J}\right][(\Delta_\eta U)_{ij} - (\Delta_\eta U)_{ij-1}]$$

or, if $\bar{v}_{ij} < 0$,

$$U_{\eta,ij} = U_{ij+1} - U_{ij} - \left[\frac{1}{2} + \frac{\Delta t\bar{v}_{ij}}{2J}\right][(\Delta_\eta U)_{ij+1} - (\Delta_\eta U)_{ij}]$$

where $\Delta_\eta U$ denotes a monotonized central difference approximation in the η direction with all quantities evaluated at t^n.

Corrector

In the corrector step we compute $\bar{u}U_\xi + \bar{v}U_\eta$ from the predicted values defined by Eq. (12). (For the remainder of this section we suppress $n+1/2$ superscripts.) The form of the corrector is motivated by a physical space interpretation of the matrix T used to define $\bar{U}$. For example, consider $\bar{u} = (y_\eta, -x_\eta)^t\cdot U$ at edge $i+1/2$,

j. If we let $(X_\eta)_{i+1/2,\,j} = X_{i+1/2,\,j+1/2} - X_{i+1/2,\,j-1/2}$, we see that $(X_\eta)_{i+1/2,\,j}$ is tangent to the edge with magnitude equal to the length of the edge. Consequently, $\bar{u}_{i+1/2,j}U_{i+1/2,j}$ represents the flux of U through edge $i+1/2, j$. This suggests the following finite volume type differencing for the corrector:

$$(\bar{u}U_\xi + \bar{v}U_\eta)_{ij} \approx (1/2)(\bar{u}_{i+1/2,\,j} + \bar{u}_{i-1/2,\,j})(U_{i+1/2,\,j} - U_{i-1/2,\,j}) + (1/2)\,(\bar{v}_{i,\,j+1/2} + \bar{v}_{i,\,j-1/2})\,(U_{i,\,j+1/2} - U_{i,\,j-1/2}) \tag{13}$$

where $\bar{u}$ and $\bar{v}$ are the appropriately scaled normal velocities at ξ = const and η = const edges, respectively.

Before evaluating the flux we must first resolve the ambiguities in edge values introduced by Eq. (12). In particular, the characteristic extrapolation has defined double values of U for each edge corresponding to expansions from either side of the interface. We will restrict the discussion to the computation of $\bar{u}_{i+1/2,\,j}$ and $U_{i+1/2,\,j}$ for edge $i+1/2, j$ from the left and right states $U^L_{i+1/2,\,j}$ and $U^R_{i+1/2,\,j}$. If we transform the Navier-Stokes equations to a local Cartesian coordinate system defined by the edge and its normal, we see that $\bar{u}$ satisfies

$$\bar{u}_t + \bar{u}\bar{u}_\chi = R \tag{14}$$

where χ is the direction normal to the edge. Here, R represents the diffusion term, the pressure gradient, and the transverse flux. Thus, $\bar{u}$ satisfies the quasilinear form of Burgers' equation with forcing terms in the direction normal to the edge. This suggests upwinding $\bar{u}$ based on the Riemann problem for Burgers' equations, namely,

$$\bar{u}_{i+1/2,\,j} = \begin{cases} \bar{u}^L & \text{if } \bar{u}^L \geq 0, \quad \bar{u}^L + \bar{u}^R \geq 0 \\ 0 & \text{if } \bar{u}^L < 0, \quad \bar{u}^R > 0 \\ \bar{u}^R & \text{otherwise} \end{cases}$$

(We suppress the $i+1/2, j$ spatial indices on left and right states here and for the remainder of the discussion.) We now upwind U based on $\bar{u}$,

$$U_{i+1/2,\,j} = \begin{cases} U^L & \text{if } \bar{u}_{i+1/2,\,j} > 0 \\ U^R & \text{if } \bar{u}_{i+1/2,\,j} < 0 \\ (1/2)\,(U^L + U^R) & \text{if } \bar{u}_{i+1/2,\,j} = 0 \end{cases}$$

Note that the form of the differencing in Eq. (13) requires a value for $U_{i+1/2,\,j}$ even in "sonic" cases in which $\bar{u}_{i+1/2,\,j} = 0$.

The Godunov method is an explicit difference scheme and, as such, requires a time-step restriction. A linear, constant-coefficient analysis shows that we must require

$$\max_{ij}\left(\frac{\bar{u}_{ij}\Delta t}{J_{ij}}, \frac{\bar{v}_{ij}\Delta t}{J_{ij}}\right) \leq 1 \tag{15}$$

for stability. The time-step restriction of the Godunov method is used to set the time step for the overall algorithm.

IV. Discretization of the Projection

In this section a numerical procedure is described for decomposing a discrete vector field into its divergence-free and gradient components. Discrete vector decompositions of this type typically require that the difference schemes used to approximate the divergence and gradient yield skew adjoint operators over appropriate finite dimensional inner product spaces of discrete scalar and vector fields. This is analogous to the situation in the continuous case when the vector and scalar fields have square integrable first-order partial derivatives and satisfy specific conditions on the boundary of the domain. The discrete divergence and gradient operators used here are similar to those considered by Stephens et. al.[11] In the decomposition of Ref. 11, the divergence-free velocity component is determined directly by a Galerkin procedure using a local basis for the subspace of discretely divergence-free vector fields.

An alternative procedure is to compute the gradient component directly. This approach has been used, for example, by van Kan,[4] Chorin,[5] and Kim and Moin[7] in connection with other divergence-gradient operator pairs. For the present divergence-gradient operator pair, the Galerkin procedure for the divergence-free component often results in a slightly smaller matrix inversion problem than that for the direct computation of the gradient component. However, the matrix for the Galerkin procedure is more complex when multiply connected domains are considered due to the appearance of nonlocal basis elements for the divergence-free subspace. For this reason, the decomposition used here will be via the direct determination of the gradient component. An alternative Galerkin projection algorithm applicable in the present context for simply connected domains is given in Ref. 12.

The discrete divergence is defined on the dual grid system of Fig. 1 by transforming to computational space and using conventional difference approximations. Thus, $\nabla \cdot U \approx DU \equiv J^{-1}\bar{D}\bar{U}$, where $\bar{D}$ is a centered approximation to $\nabla_\Xi \cdot$ defined by

$$[\bar{D}\bar{U}]_{i+1/2,\,j+1/2} \equiv (1/2)\,[(\bar{u}_{i+1,\,j+1} - \bar{u}_{i,\,j+1}) + (\bar{u}_{i+1,\,j} - \bar{u}_{ij}) + (\bar{v}_{i+1,\,j+1} - \bar{v}_{i+1,\,j}) + (\bar{v}_{i,\,j+1} - \bar{v}_{ij})] \tag{16}$$

Recall that $\bar{U}_{ij} = T_{ij}U_{ij}$, where the matrices T_{ij} are evaluated using the finite difference approximations described in the preceding section. These difference approximations were chosen to ensure that a uniform vector field U_∞ will satisfy $DU_\infty = 0$, regardless of the grid being used.

We now define a discrete gradient operator that is numerically consistent with the pressure gradient term in Eq. (3) and is skew adjoint to D. Consider a domain covered by the staggered grid system with the indices $i = 0$, $i = N$, $j = 0$, and $j = M$ corresponding to the outer boundaries of the domain in physical space. The inner boundary γ (when present) is represented by the union of disjoint closed curves each of which corresponds in the Ξ space to an internal branch slit lying on a segment of a primary grid line. For the present applications, we assume that each subcurve of the inner boundary represents a stationary impermeable body and, thus, the discrete velocity field satisfies $U_{ij} = 0$ when $X_{ij} \in \gamma$. Under this condition, $\bar{D}$ satisfies the summation-by-parts identity

$$\sum_{i=0}^{N-1}\sum_{j=0}^{M-1}[(\bar{D}\bar{U})\phi]_{i+1/2,\,j+1/2} = -\sum_{i=0}^{N}\sum_{j=0}^{M}\bar{U}_{ij}\cdot[\bar{G}(E\phi)]_{ij} \tag{17}$$

where

$$(\bar{G}\phi)_{ij} = \frac{1}{2}\begin{bmatrix}\phi_{i+1/2,\,j+1/2} - \phi_{i-1/2,\,j+1/2} + \phi_{i+1/2,\,j-1/2} - \phi_{i-1/2,\,j-1/2} \\ \phi_{i+1/2,\,j+1/2} - \phi_{i+1/2,\,j-1/2} + \phi_{i-1/2,\,j+1/2} - \phi_{i-1/2,\,j-1/2}\end{bmatrix}$$

and $E\phi$ is the extension of ϕ by zero [i.e., $(E\phi)_{i+1/2,\,j+1/2} = \phi_{i+1/2,\,j+1/2}$ for $i = 0, \ldots, N-1$; $j = 0, \ldots, M-1$; and $E\phi = 0$ elsewhere]. Note that the operator $\bar{G}$ is a centered difference approximation to ∇_Ξ at nodes not on the boundaries. The identity equation (17) and the definition of D imply that

$$\sum_{i=0}^{N-1}\sum_{j=0}^{M-1}J_{i+1/2,\,j+1/2}[(DU)\phi]_{i+1/2,\,j+1/2} = -\sum_{i=0}^{N}\sum_{j=0}^{M}U_{ij}\cdot[T^t\bar{G}(E\phi)]_{ij} \tag{18}$$

Note that the values of the metric coefficients on the inner boundary γ do not appear in Eq. (18) since they are multiplied by zero.

The discrete gradient G, defined by

$$(G\phi)_{ij} \equiv \begin{cases} J_{ij}^{-1} T_{ij}^{t} [\bar{G}(E\phi)]_{ij} & \text{if } X_{ij} \notin \gamma \\ 0 & \text{if } X_{ij} \in \gamma \end{cases} \tag{19}$$

represents a centered difference approximation to $J^{-1}T^{t}\nabla_{\Xi}\phi$ at nodes not on the boundaries. Furthermore, it follows from Eqs. (18) and (19) that G and D are skew adjoint with respect to the spaces and inner products defined as follows. Let $\boldsymbol{V}$ denote the space of discrete vectors

$$\{U_{ij}:\ i = 0, \ldots, N;\quad j = 0, \ldots, M;\quad U_{ij} = 0 \quad \text{when} \quad X_{ij} \in \gamma\}$$

and W the space of discrete scalars

$$\{\phi_{i+1/2, j+1/2}:\ i = 0, \ldots, N-1;\quad j = 0, \ldots, M-1\}$$

with inner products

$$(\phi, \theta)_W \equiv \sum_{i=0}^{N-1} \sum_{j=0}^{M-1} J_{i+1/2, j+1/2} \phi_{i+1/2, j+1/2} \theta_{i+1/2, j+1/2}$$

and

$$(U, V)_V \equiv \sum_{i=0}^{N} \sum_{j=0}^{M} J_{ij} (U_{ij} \cdot V_{ij})$$

on W and $\boldsymbol{V}$, respectively. Then,

$$(DU, \phi)_W = -(U, G\phi)_V \tag{20}$$

for all $U \in \boldsymbol{V}$ and $\phi \in W$.

The specific form of the discrete decomposition depends on the conditions imposed at the outer boundary for the problem under consideration. In this paper, we consider a class of problems for which the velocity is specified on a portion of the outer boundary Γ_D, whereas the remainder of this boundary represents an outflow condition. For simply connected domains, discrete Galerkin projections for problems of this type with the outflow modeled using homogeneous Neumann conditions on the velocity have been considered by Solomon and Szymczak.[13] In the formulation of Ref. 13 the specified Dirichlet data must satisfy compatibility conditions associated with the discrete divergence condition. The present treatment of the outflow boundary differs from that of Ref. 13 in that no conditions are explicitly imposed on the velocity at an outlet and there are no compatibility conditions on the specified data. The present treatment is analogous to imposing "natural" boundary conditions in a variational form for the projection.

The problem can be reduced to one with homogeneous data on Γ_D by subtracting a boundary mesh vector $V_B \in \boldsymbol{V}$ satisfying the specified Dirichlet data on Γ_D and $DV_B = 0$. A procedure for computing such boundary mesh vectors is described in Refs. 11 and 13, although this explicit construction is not necessary in the present formulation. Since the intermediate velocity U^* satisfies the Dirichlet conditions, it follows that

$$U^* - V_B \in \boldsymbol{V}^0 \equiv \{V \in \boldsymbol{V}: V = 0 \quad \text{on} \quad \Gamma_D\}$$

To obtain an orthogonal decomposition of $\boldsymbol{V}^0$, we apply Eq. (20) to $V \in \boldsymbol{V}^0$ and $\phi \in W$ to obtain

$$(DV, \phi)_W = -(V, G^0\phi)_V \tag{21}$$

where G^0 is defined to be zero on Γ_D and given by Eq. (19), elsewhere. Therefore, we have the direct sum decomposition of $\boldsymbol{V}^0 = \boldsymbol{D} + \boldsymbol{G}$ where $\boldsymbol{D} = \ker D \cap \boldsymbol{V}^0$ and $\boldsymbol{G} = \text{range } G^0$. It follows that for $U \in \boldsymbol{V}$ and satisfying the Dirichlet conditions on Γ_D

$$U - V_B = U_d + G^0\phi \tag{22}$$

where $U_d \in \boldsymbol{D}$ and $\phi \in W$. Note that the boundary mesh vector V_B is not unique, however, the sum $V_B + U_d$ is uniquely determined regardless of the choice of V_B. Therefore, we can write $PU = V_B + U_d = U - G^0\phi$.

To determine the $G^0\phi$ component, we note that $\phi \in W$ is given by

$$\phi = \sum_{i=0}^{N-1} \sum_{j=0}^{M-1} \phi_{i+1/2, j+1/2} \Phi^{i+1/2, j+1/2}$$

where $\{\Phi^{k+1/2, l+1/2} \in W:\ k = 0, \ldots, N-1;\ l = 0, \ldots, M-1\}$ is the local basis for W defined by $\Phi^{k+1/2, l+1/2}_{i+1/2, j+1/2} = \delta_{ik}\,\delta_{jl}$ (δ_{ij} is the Kronecker delta). It follows from Eq. (22) that ϕ satisfies $DG^0\phi = DU$ which, by Eqs. (20) and (21), is equivalent to the following symmetric linear system for the coefficients $\phi_{i+1/2, j+1/2}$:

$$\sum_{i=0}^{N-1} \sum_{j=0}^{M-1} \phi_{i+1/2, j+1/2} (G^0\Phi^{i+1/2, j+1/2}, G^0\Phi^{k+1/2, l+1/2})_V = (U, G\Phi^{k+1/2, l+1/2})_V \tag{23}$$

where $k = 0, \ldots, N-1$, $l = 0, \ldots, M-1$. The linear system (23) has an algebraic structure of the type associated with a nine point discretization of the transformed Laplacian. In our computations, this system is solved using a preconditioned conjugate gradient algorithm with a modified incomplete lower-upper preconditioner with zero fill [MILU(0)], see e.g., Ref. 14. This procedure comprises the bulk of the computational work of the algorithm.

V. Numerical Results

In this section we present computational results illustrating the performance of the method. The first example is flow over a cylinder at $Re = 140$. Uniform horizontal flow conditions ($u = 1$, $v = 0$) were specified along the top, bottom, and left boundaries corresponding to a cylinder pulled through a quiescent fluid in a channel. The fluid is viewed in the frame of reference moving with the cylinder. The initial conditions are $u = 1$, $v = 0$ at all points except those on the cylinder (where $u = v = 0$ for all time), corresponding to an impulsively started cylinder. A small vortex was included in the initial data upstream of the cylinder to facilitate the rapid initialization of the shedding process. A section of the channel 32 cylinder diameters long and 16 diameters wide was discretized with a 600×300 grid using a biharmonic grid generation algorithm.[15] No clustering terms were used so the grid is essentially uniformly distributed. Figure 2 displays contours of vorticity and concentration of a scalar quantity ("dye") which is passively advected by the velocity field. This scalar quantity was initially set to zero at all points except those on or adjacent to the cylinder, where it was maintained at a constant (boundary) value of one, corresponding to dye being injected into the flowfield from the cylinder wall. One cycle of periodic vortex shedding is displayed in this figure, which is in good qualitative agreement with the photographs of experimental results displayed, e.g., in Ref. 16.

A time history of the v-velocity component at points 1 diameter above the centerline, and 5 and 10 cylinder diameters downstream from the cylinder is shown in Fig. 3. The Strouhal number for this computation is 0.186 compared to the value of 0.180 determined through the careful measurements of Williamson.[17] Additional computations suggest that the Strouhal number is strongly dependent on the width of the channel, and we believe the relatively narrow channel used for this example accounts for the discrepancy. A more thorough study of computing Strouhal numbers, including

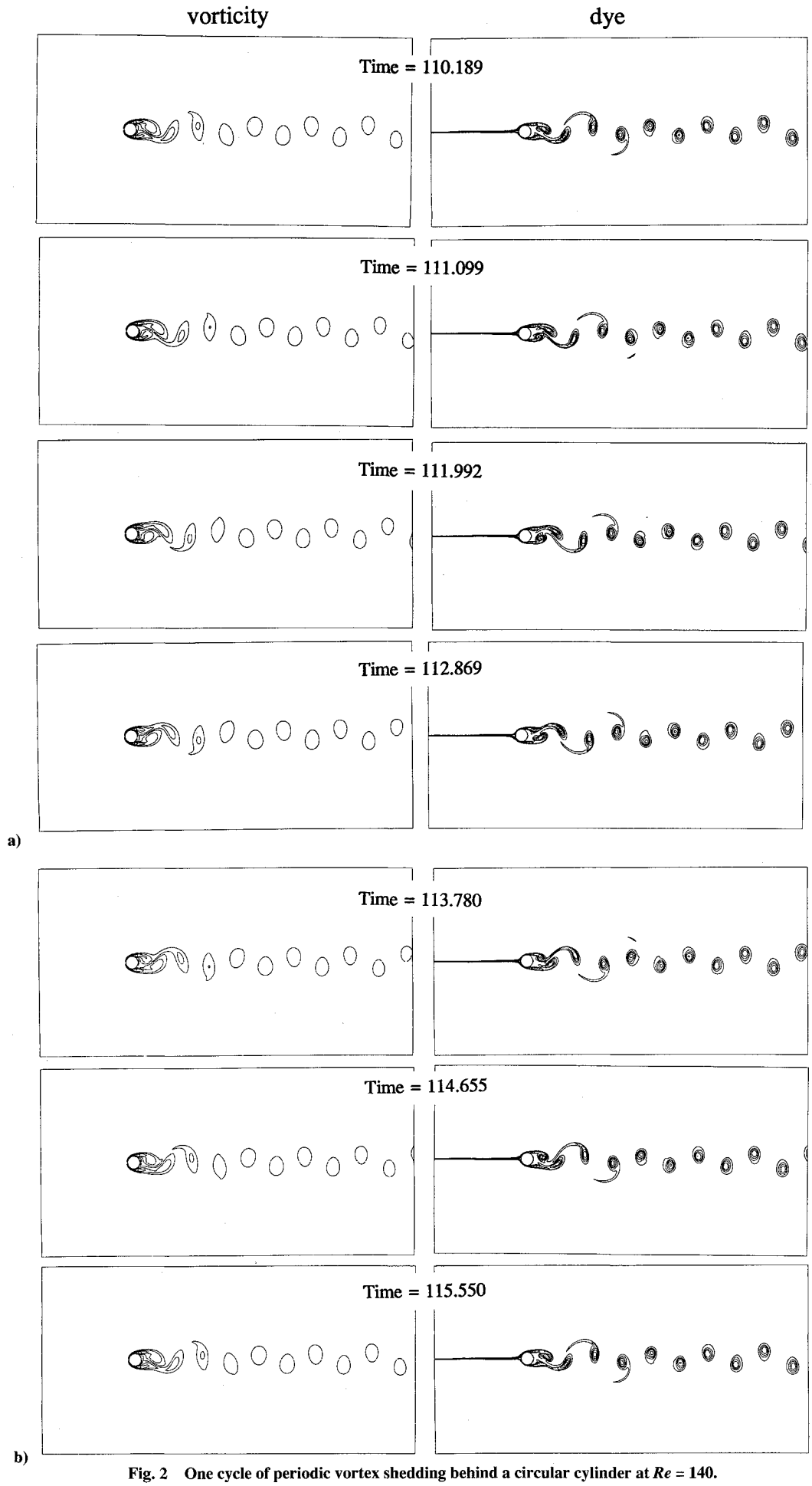

Fig. 2 One cycle of periodic vortex shedding behind a circular cylinder at $Re = 140$.

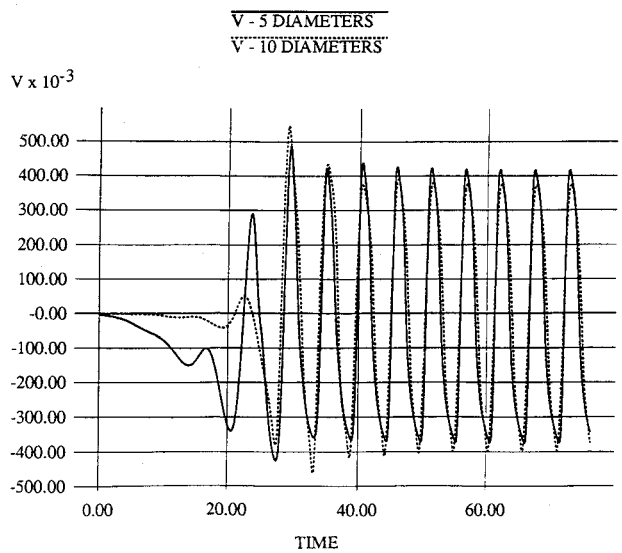

Fig. 3 Time history of *v*-velocity components for the flow depicted in Fig. 2; velocities were computed along the centerline at distances of 5 and 10 cylinder diameters downstream from the cylinder.

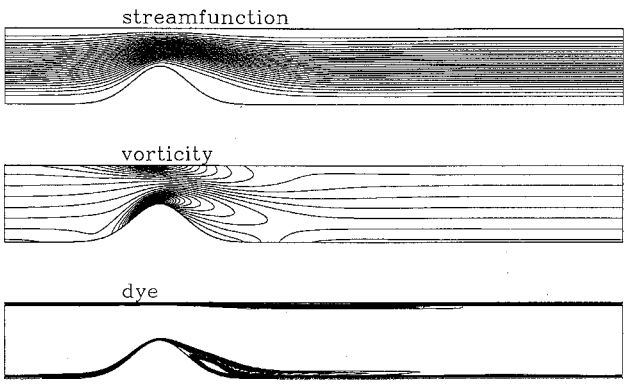

Fig. 4 Steady flow in a constricted channel at *Re* = 50.

the dependence on the grid size and locations of the boundaries, will appear in a forthcoming paper.

Our second example is flow in a channel with a constriction. The constriction is given by a smooth Gaussian profile which, at its maximum extent, reduces the width of the channel by a factor of 2. A coarse 200×25 and a fine 400×50 grid were generated using the same biharmonic grid generation algorithm (appropriately modified) as in the preceding example. Once again, no clustering terms were used so the grids are essentially uniformly distributed. Boundary conditions for parabolic inflow and no slip walls were imposed. The flow was initialized by the parabolic inflow profile along constant ξ lines in the computational space. Computations were performed for $Re = 50$, 500, and 5000, where Re is based on the maximum inlet velocity and the channel width.

For $Re = 50$ the steady-state solution (attained after 2000 time steps on the fine grid) is shown in Fig. 4, which shows a small recirculation region behind the constriction. (For these problems the dye is injected at grid points adjacent to the channel walls.) Figure 5 shows the steady-state solution obtained on the fine grid for $Re = 500$ flow. The recirculation region behind the bump extends a distance 4.74 (9.48 bump heights). On the coarse grid this region extended a distance of 4.68 (9.36 bump heights). A second recirculation region also exists (with each grid) along the top of the channel and extends out of the domain. Similar phenomena were reported by Armaly et al.[18] for the backward facing step at a comparable Reynolds number. Figure 6 shows the time histories of the *u*-velocity component at a point in the center of the channel a distance of four bump heights behind the bump. This figure clearly indicates convergence to a steady state, however, the number of time steps required to be within some small tolerance of the asymptotic value is about 10 times as many as was needed for the $Re = 50$ case.

Contours of the dye in the fluid are displayed in Fig. 7 for the fine grid solution at $Re = 5000$. This Reynolds number is well into the turbulent regime, and the resulting flow is quite complex. The dominant features of the flow are the large vortices being alternately shed from the top and bottom walls. A number of smaller secondary structures are also apparent. The flow directly behind the constriction is particularly complex, involving a number of

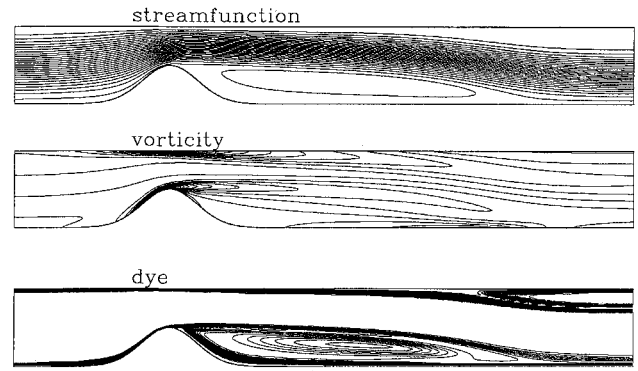

Fig. 5 Steady flow in a constricted channel at *Re* = 500.

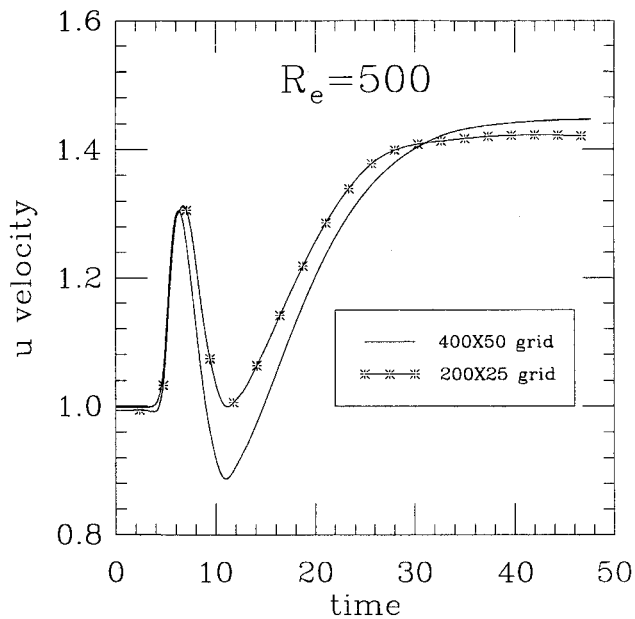

Fig. 6 Time history of a *u*-velocity component for the flow depicted in Fig. 5; velocity was computed in the center of the channel at a distance of four bump heights downstream from the bump.

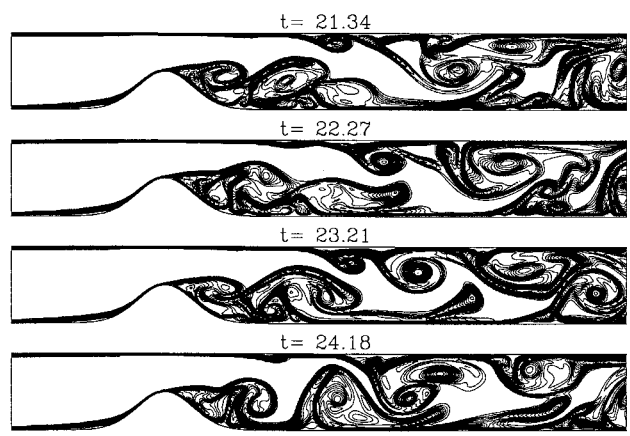

Fig. 7 Time sequence of dye contours for flow in a constricted channel at *Re* = 5000.

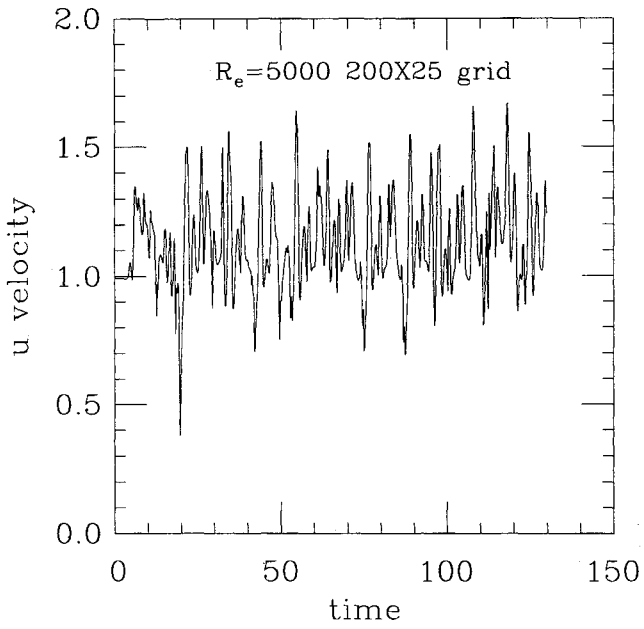

Fig. 8 Time history of a u-velocity component for the coarse (200 × 25) grid solution in a constricted channel at Re = 5000; velocity was measured at the same point as in Fig. 6.

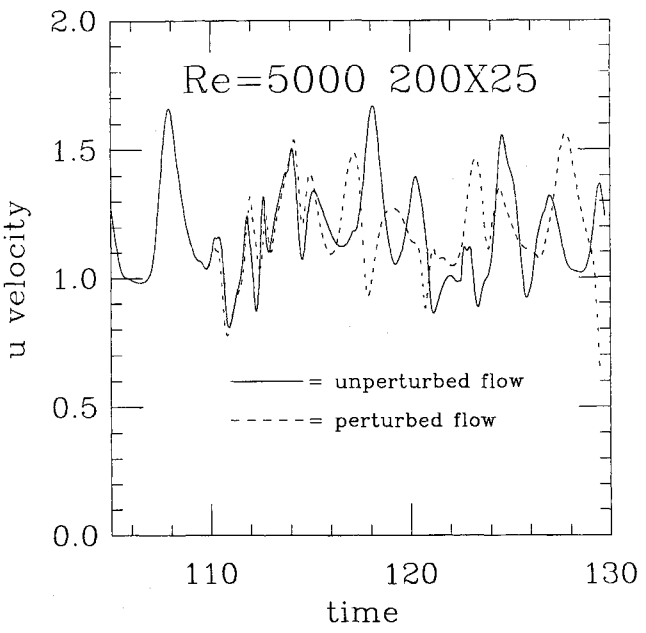

Fig. 9 Comparison of the time histories of a u-velocity component for perturbed and unperturbed flow in a constricted channel; perturbation was a 1% increase in the u-component of velocity at one point above the bump at time t = 86.6.

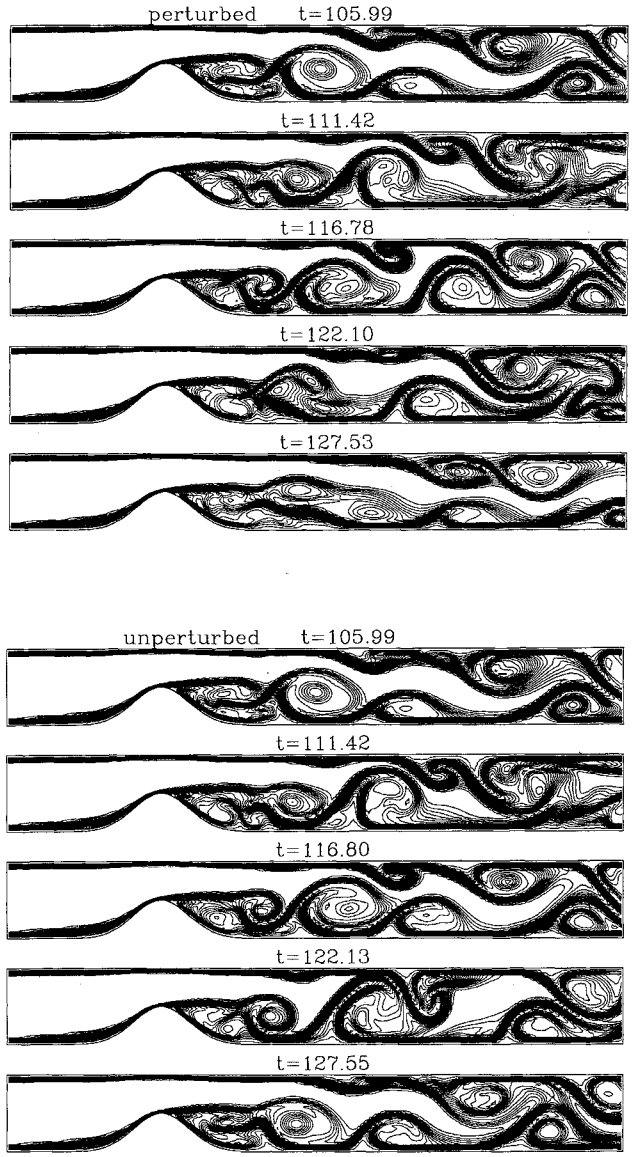

Fig. 10 Comparison of dye contours for the unperturbed and perturbed flowfields in the constricted channel at Re = 5000 (coarse grid solutions).

counter-rotating vortices that participate in the shedding cycle. We remark that despite cell Reynolds numbers exceeding 100, spurious numerical oscillations do not appear upstream of the bump. These oscillations could be expected for centered difference discretizations (cf., Ref. 19).

To study the long-time behavior of this problem we returned to the coarse grid where the dominant features of the vortex shedding persisted. Figure 8 shows the time history of the u-velocity component (at the same location as in Fig. 6). This history corresponded to 12,000 time steps at a Courant number of 0.5. No asymptotic or periodic behavior is evident from these results. The stability of the flowfield was examined numerically by restarting the computations at time step 8000 (t = 86.6) with a 1% perturbation of the u-velocity component at a point above the bump in the center of the channel. A comparison of the time histories of the perturbed and unperturbed problems is shown in Fig. 9. At about t = 110 the histories rapidly diverge from each other. Figure 10 compares the corresponding dye plots of the perturbed and unperturbed flowfields at several times. This observed sensitivity to small perturbations of the initial data is indicative of chaotic behavior. The absence of numerical oscillations (on the order of the grid size) in the vicinity of the bump suggests that this long-time behavior is not due to "numerical turbulence" (see, e.g., Ref. 20). However, a more detailed study of this phenomena will appear elsewhere.

Assessing the computational efficiency of the algorithm requires some caution. The dominant cost in the algorithm is the solution of the linear system associated with the projection. This system is solved iteratively, and the performance of the iterative method depends on a number of factors including the problem size, the complexity of the flow, the boundary conditions, and the level of distortion of the grid. For the constricted channel problem described the method required approximately 25 μs per zone on a Cray X-MP using one processor. This figure is based on the time spent in the main integration loop during the first 20 time steps at Reynolds number 500 and does not include initialization, grid generation, and other start-up costs. This particular case is ideally

suited to the method and typical timings are likely to be somewhat higher.

VI. Conclusions

In this paper we have described a numerical method for solving the incompressible Navier-Stokes equations on a logically rectangular quadrilateral grid. The method uses a second-order projection formulation and incorporates a Godunov-type discretization of the convective terms that is second-order accurate for smooth flow and is sufficiently robust to treat strongly sheared flows without loss of stability or oscillations independent of Reynolds number. The projection procedure described in this paper is suitable for multiply connected domains and is readily extendible for three-dimensional problems.

Acknowledgments

The work of the first author was performed under the auspices of the U.S. Department of Energy by the Lawrence Livermore National Laboratory under Contract W-7405-Eng-48. Partial support under Contract W-7405-Eng-48 was provided by the Applied Mathematical Sciences Program of the Office of Energy Research and by the Defense Nuclear Agency under IACRO 92-825. The work of the second and third authors was supported by the Naval Surface Warfare Center Independent Research Fund.

References

[1]Bell, J. B., Colella, P., and Glaz, H. M., "A Second-Order Projection Method for Viscous, Incompressible Flow," AIAA Paper 87-1176, June 1987.

[2]Bell, J. B., Colella, P., and Glaz, H. M., "A Second-Order Projection Method for the Incompressible Navier-Stokes Equations," *Journal of Computational Physics*, Vol. 85, No. 2, 1989, pp. 257–283.

[3]Bell, J. B., Glaz, H. M., Solomon, J. M., and Szymczak, W. G., "Application of a Second-Order Projection Method to the Study of Shear Layers," *Proceedings of the 11th International Conference on Numerical Methods in Fluid Dynamics*, edited by D. L. Dwoyer, M. Y. Hussaini, and R. G. Voigt, Lecture Notes in Physics, Vol. 323, Springer-Verlag, Berlin, 1989, pp. 142–146.

[4]Van Kan, J., "A Second-Order Accurate Pressure-Correction Scheme for Viscous Incompressible Flow," *Journal of Scientific and Statistical Computing*, Vol. 7, July 1986, pp. 870–891.

[5]Chorin, A. J., "On the Convergence of Discrete Approximations to the Navier-Stokes Equations" *Mathematics of Computation*, Vol. 23, April 1969, pp. 341–353.

[6]Temam, A. R., *Navier-Stokes Equations*, North-Holland, Amsterdam, 1984, Chaps. 1, 7.

[7]Kim, A. J., and Moin, P., "Application of a Fractional-Step Method for Incompressible Navier-Stokes Equations," *Journal of Compututational Physics*, Vol. 59, No. 2, 1985, pp. 308–323.

[8]Steger, J. L., "Implicit Finite Difference Simulation of Flow About Arbitrary Geometrics with Application to Airfoils," AIAA Paper 77-665, June 1977.

[9]Colella, P., "Multidimensional Upwind Methods for Hyperbolic Conservation Laws," *Journal of Compututational Physics*, Vol. 87, March 1990, pp. 171–200.

[10]Van Leer, B., "Multidimensional Explicit Difference Schemes for Hyperbolic Conservation Laws," *Computing Methods in Applied Sciences and Engineering*, Vol. VI, edited by E. R. Glowinski and J.-L. Lions, North-Holland, Amsterdam, 1984, pp. 493–499.

[11]Stephens, A. B., Bell, J. B., Solomon, J. M., and Hackerman, L. B., "A Finite Difference Galerkin Formulation of the Incompressible Navier-Stokes Equations," *Journal of Compututational Physics*, Vol. 53, Jan. 1984, pp. 152–172.

[12]Bell, J. B., Solomon, J. M., and Szymczak, W. G., "A Second-Order Projection Method for the Incompressible Navier Stokes Equations on Quadrilateral Grids," AIAA Paper 89-1967, June 1989.

[13]Solomon, J. M., and Szymczak, W. G., "Finite Difference Solutions for the Incompressible Navier-Stokes Equations using Galerkin Techniques," *Advances in Computer Methods for Partial Differential Equations*, Vol. V, edited by E. R. Vichnevetsky and R. S. Stepleman, IMACS, 1984, pp. 174–182.

[14]Axelsson, O., and Lindskog, G., "On the Eigenvalue Distribution of a Class of Preconditioning Methods," *Numerische Mathematik*, Vol. 48, No. 5, 1986, pp. 479–498.

[15]Bell, J. B., Shubin, G. R., and Stephens, A. B., "A Segmentation Approach to Grid Generation Using Biharmonics," *Journal of Compututational Physics*, Vol. 47, No. 3, 1982, pp. 463–472.

[16]Van Dyke, M., *An Album of Fluid Motion*, Parabolic Press, Stanford, CA, 1982, p. 56.

[17]Williamson, C. H. K., "Oblique and Parallel Modes of Vortex Shedding in the Wake of a Circular Cylinder at Low Reynolds Numbers," *Journal of Fluid Mechanics*, Vol. 206, Sept. 1989, pp. 579–627.

[18]Armaly, B. F., Durst, F., Pereira, J. C. F., and Schonung, B., "Experimental and Theoretical Investigation of Backward-Facing Step Flow," *Journal of Fluid Mechanics*, Vol. 127, Feb. 1983, pp. 473–496.

[19]Szymczak, W. G., Solomon, J. M., Berger, A. E., Bell, J. B., and Osborn, J. E., "Numerical Solutions for Laminar Flow over a Backward-Facing Step," *Advances in Computer Methods for Partial Differential Equations*, Vol. VI, edited by E. R. Vichnevetsky and R. S. Stepleman, IMACS, 1987, pp. 517–524.

[20]Zang, T. A., Krist, S. E., and Hussaini, M. Y., "Resolution Requirements for Numerical Simulations of Transition," ICASE Rept. 89-9, Hampton, VA, Jan. 1989.